

Understanding the Effect of Saturated Gases on Catalytic Performance of Graphitic Carbon Nitride (g-C₃N₄) for H₂O₂ Generation and Dye Degradation in the Presence of Ultrasound

A. Karunakaran, Hoang-Duy P. Nguyen, Chris R. Bowen,* Frank Marken, Bastola Narayan, Steve Dunn, Yan Zhang, Miao Jia, Yan Zhao, Nguyen-Phuong Nguyen, Bao-Ngoc T. Le, and Thuy-Phuong T. Pham*

In this article, the effect of saturated gases on H₂O₂ generation and dye degradation is examined using graphitic carbon nitride (g-C₃N₄) as a piezoelectric catalyst. A detailed catalytic evaluation is carried out using a double-bath sono-reactor, where the performance of g-C₃N₄ for H₂O₂ production and degradation of rhodamine B and indigo carmine dyes is evaluated for a range of catalyst dosage levels and saturated gases. Specific gases are selected to understand their role in the sonochemical production of reactive oxygen species (ROS) and reactive nitrogen species (RNS) and to elucidate the catalytic mechanism. The use of an Ar–O₂ gas mixture leads to the highest yield for H₂O₂ production and dye degradation due to the positive effect of argon and oxygen in the generation of H₂O₂ and ROS, respectively. The presence of nitrogen in both air and in an Ar–air mixture increases H₂O₂ generation since RNS improves the conversion of •OH into H₂O₂. In contrast, air and Ar–air negatively influences the generation of ROS, which results in a low rate of dye degradation. In this work, new insights of the mechanisms of sonochemical and piezocatalytic processes in the use of graphitic carbon nitride in catalytic applications are provided.

1. Introduction

As a fascinating metal-free conjugated polymer semiconductor, 2D graphitic carbon nitride (g-C₃N₄) has been widely investigated as a photocatalyst.^[1–3] Generally, g-C₃N₄ is recognized as a nontoxic and low-cost material, which can be produced at relatively low temperatures.^[4] In addition, it exhibits appealing properties, which include good thermal and chemical stability, and a unique band structure.^[3,5] As a result, it has shown intriguing prospects both in the photocatalytic production of H₂O₂,^[6] which is globally recognized as an indispensable chemical^[7,8] and the degradation of dyes for water treatment applications.^[9] However, the catalytic performance of pristine g-C₃N₄ is limited by the rapid recombination of photoinduced electron–hole pairs, its limited surface area, and low sunlight absorption.^[10] Moreover,

as with most photocatalysts which are used without dye modification, pure g-C₃N₄ suffers from the disadvantage of a low utilization of visible light, which limits its practical applications.^[11]

A. Karunakaran, C. R. Bowen, F. Marken, B. Narayan
Department of Mechanical Engineering
University of Bath
Bath BA2 7AY, UK
E-mail: msscrb@bath.ac.uk

H.-D. P. Nguyen, N.-P. Nguyen, B.-N. T. Le, T.-P. T. Pham
Institute of Chemical Technology
Vietnam Academy of Science and Technology
1A TL29 Street, HCM City 729110, Vietnam
E-mail: pttphuong@ict.vast.vn

 The ORCID identification number(s) for the author(s) of this article can be found under <https://doi.org/10.1002/adem.202301958>.

© 2024 The Authors. Advanced Engineering Materials published by Wiley-VCH GmbH. This is an open access article under the terms of the Creative Commons Attribution License, which permits use, distribution and reproduction in any medium, provided the original work is properly cited.

DOI: 10.1002/adem.202301958

S. Dunn
School of Engineering
London South Bank University
103 Borough Road, London SE1 0AA, UK

Y. Zhang, M. Jia, Y. Zhao
Powder Metallurgy Institute
State Key Laboratory of Powder Metallurgy
Changsha 410083, China

N.-P. Nguyen, T.-P. T. Pham
Graduate University of Science and Technology
Vietnam Academy of Science and Technology
18 Hoang Quoc Viet Street, Cau Giay District, Hanoi 122000, Vietnam

To improve the efficiency, researchers have recently focused on the use of photocatalysts that possess piezo- or pyroelectric properties, which can aid in the harvesting of alternative ambient energy sources, such as mechanical forces or heat energy from sunlight and low-grade thermal sources.^[12,13]

While graphitic carbon nitride is an inherently non-piezoelectric material, an apparent piezoelectric response can be revealed through a change in symmetry.^[14] Sharma et al. theoretically^[15] and experimentally^[16] demonstrated that a non-piezoelectric material can possess an apparent piezoelectricity due to flexoelectricity as a result of non-centrosymmetric pores and nanoscale size effects. Specifically, 2D g-C₃N₄ which contains graphitic carbon nitride nanosheets has been experimentally shown to exhibit piezoelectric e_{11} coefficients (a measure of the charge density per unit strain) of 0.758 C m⁻², which is higher than quartz.^[16] The use of a g-C₃N₄ material can also significantly increase the exposed surface area, accessible channels, and active edges, thereby promoting charge separation, molecular mass transfer, and surface reactions.^[17] Most of these outstanding properties benefit the catalytic properties of this fascinating material for energy-related applications.

Recent interest has led to the examination of the potential of graphitic carbon nitride to produce hydrogen peroxide and degrade water pollutants when used as either a piezocatalyst^[4,18–20] or a piezophotocatalyst.^[21–23] However, studies to date have primarily used a high catalyst dosage, varying from 0.5^[4] to 1 g L⁻¹,^[18,19] such a high catalyst dosage level results in the need for additional stirring to prevent the catalyst from depositing at the base of the reactor. It has been reported that the use of an agitator can lead to fluctuations in the propagation of ultrasonic waves.^[24] Moreover, the incorporation of an additional stirrer into the reactor makes it complex to study the effect of dissolved gases on the piezocatalytic activity toward H₂O₂ production and pollutant degradation. This can lead to a contradiction between different studies in terms of the level H₂O₂ products, where the production rate has increased^[23] or decreased^[4,19] when using a nitrogen atmosphere, compared to that of air. In addition, our previous studies have shown that a piezocatalysis can be well dispersed, or can even form a stable nanofluid at low catalyst dosage levels that range from 0.01 to 0.1 g L⁻¹ without any additional stirring during sonication.^[25–28]

In this work, the piezocatalytic activity of the g-C₃N₄ material is examined for the generation of hydrogen peroxide (H₂O₂) and degradation of dyes, in particular the impact of saturated gases and catalyst loading on performance. Rhodamine B (RhB) and indigo carmine were selected as representatives for cationic (positively charged) and anionic (negatively charged) dyes, respectively, to understand the impact of the type of dye on the performance of g-C₃N₄; this is a relatively neutral material as its point of zero charge was reported to be 7.79.^[29] A detailed catalytic evaluation was carried out using a double-bath catalytic sono-reactor, which was custom-designed and built to minimize experimental uncertainties and ensure reproducibility. The performance of g-C₃N₄ for H₂O₂ production and degradation of RhB and indigo carmine dyes was evaluated for a range of dosage levels and saturated gases. An understanding of the piezocatalytic/piezoelectrochemical process enables advances in environmental catalytic processes by mechanical deformation of a material for charge transfer. The potential of the piezocatalytic approach for

producing hydrogen peroxide using sustainable materials is scalable and can be produced at an industrial level as a new promising approach in the direction of sustainable energy.

2. Experimental Section

2.1. Synthesis of Graphitic Carbon Nitride (g-C₃N₄)

Generally, g-C₃N₄ could be synthesized by pyrolysis of nitrogen-rich precursors, where graphitic carbon nitride was prepared from melamine, following the literature,^[4,30] by heating in a gas-exchanging alumina crucible in the tube furnace at 540 °C for 4 h. As outlined in **Figure 1a**, during pyrolysis, the melamine polymerized into a g-C₃N₄ network and was accompanied by a color change from white to yellow, see **Figure 1b**. The furnace was allowed to cool down to room temperature before the final material was removed, and the g-C₃N₄ material had the appearance of a loose and fluffy powder, **Figure 1c**. The resultant products were collected and ground into fine particles using mortar and pestle, see **Figure 1d**.

2.2. Sono-Piezocatalytic Experiments

The experimental setup of the double-bath-type sono-reactor is shown in **Figure 2**. A 100 mL Erlenmeyer flask was fixed in an axial position located 10 mm from the bottom of a 60 W-ultrasonic cleaner bath (Taiwan Total Meter) with a designed cover to ensure experimental reproducibility. During the H₂O₂ generation experiments, a specific amount of catalyst was dispersed in 100 mL of distilled water. In the dye degradation experiments, a desired concentration of dye solution was selected.

The samples for H₂O₂ production or dye degradation were subsequently magnetically stirred and saturated with a stream of a desired gas or gas mixture composed of argon, oxygen, and nitrogen for at least 45 min prior to being sonicated. These gases were chosen to assess not only their important roles in sonochemical production of reactive oxygen species (ROS) and reactive nitrogen species (RNS), but also due to their abundance in the earth's atmosphere. It is worth noting that magnetic stirring was applied regardless of the presence and absence of a catalyst to eliminate the effect of a PTFE magnetic bar.^[31] The bubbling of gases was then continued throughout sonication to maintain the same dissolved gaseous content. Four mass flow controllers (STEC Inc., model SEC-4400R, Japan) were used to obtain the desired flow rate of individual gases, and a soap-film bubble flowmeter (Hewlett–Packard, USA) was employed to verify the total actual flow rate for all experiments. The temperature of the ultrasonic bath was maintained at an ambient temperature of 35 ± 0.5 °C using a temperature controller, which was coupled with an external thermocouple and a peristaltic pump to circulate heated water to an external cooling bath. While a high temperature could lead to a decrease in the efficiency of the ultrasonic effects, it was chosen, from the practical point of view, to demonstrate the economic feasibility of this system. The inner thermocouple was inserted into the Erlenmeyer flask only for the calorimetric measurement.

After each desired time interval, the ultrasound was turned off and 2.5 mL of reaction solution was withdrawn while remaining

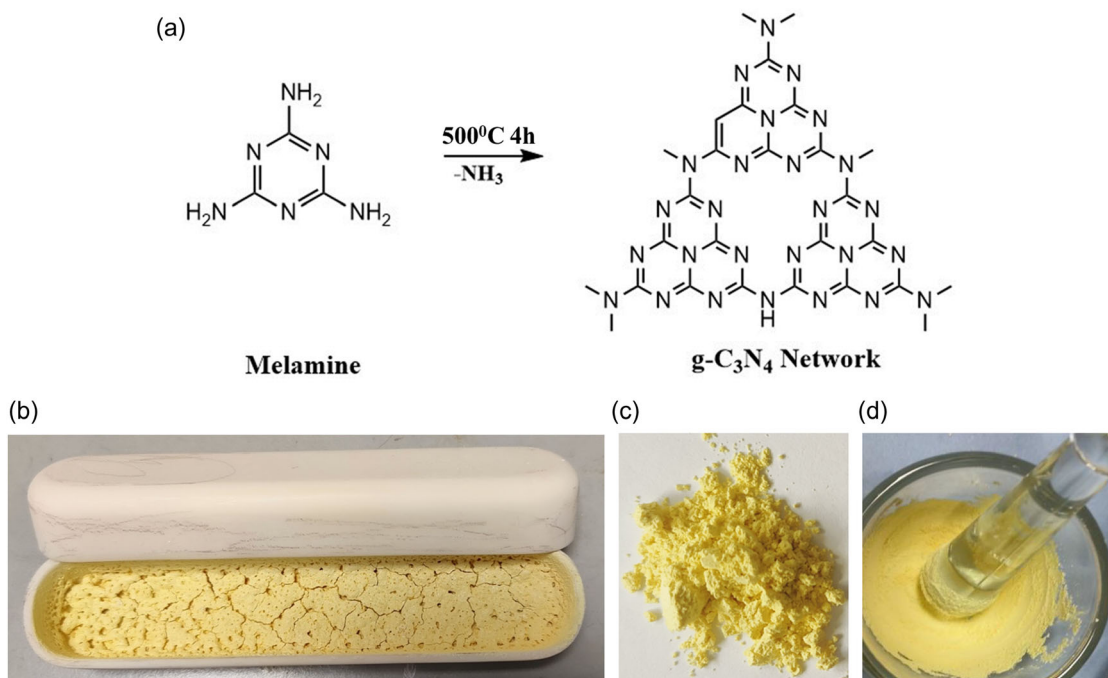


Figure 1. a) Reaction pathway of transformation of melamine to graphitic carbon nitride (g-C₃N₄) by thermal condensation. b,c) Graphitic carbon nitride (g-C₃N₄) obtained from melamine and d) g-C₃N₄ ground in mortar and pestle.

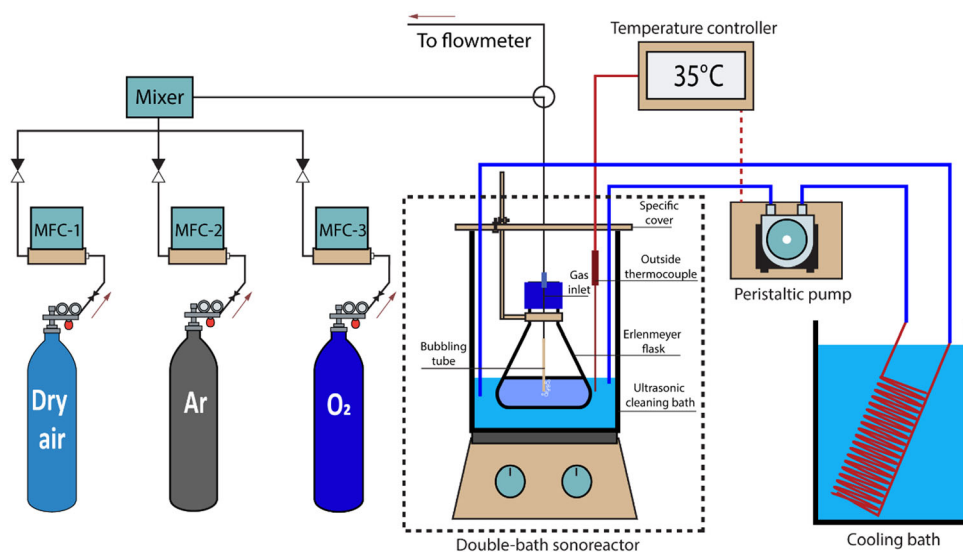


Figure 2. Schematic of experimental system based on double-bath sono-reactor for ultrasound activating water (UAW) production.

in the purging gases to ensure a consistent level of dissolved gases. It was worth noting that after each withdrawal, the mixture was magnetically stirred for 5 min to redisperse the catalyst and the total withdrawn volume did not exceed 10% of the initial volume of the reaction solution. The concentration of H₂O₂ generated during sonication was determined using the iodometric method,^[32] where iodide ion (I⁻) reacted with hydrogen peroxide to form a triiodide (I₃⁻) ion, which absorbs light at 352 nm. A 2 mL volume sample was mixed in a quartz cuvette containing 0.75 mL of

0.10 M potassium biphthalate and 0.75 mL of a solution containing 0.4 M potassium iodide, 0.06 M sodium hydroxide, and 10⁻⁴ M ammonium molybdate. The mixed solution was allowed to stand for 2 min prior to being analyzed using a HP 8453 UV-vis spectrophotometer (USA). The initial and residual concentrations of RhB and indigo carmine were determined by the same UV-vis spectroscopy at a wavelength of 554 and 610 nm, respectively.

The H₂O₂ production and pollutant degradation *rate* indicated the total amount of H₂O₂ produced and pollutant degradation per

hour (mmol h^{-1}), respectively. In addition, the *yield* indicated the amount of H_2O_2 produced or pollutant degraded per hour and per unit mass of catalyst ($\text{mmol h}^{-1} \text{g}_{\text{cat}}^{-1}$). The *yield* (Y) was calculated according to Equation (1):

$$Y = \frac{(R_c - R_b)}{m_c} \times 100\% \quad (1)$$

where R_c and R_b are the production/degradation rate in the presence and absence of catalyst (mmol h^{-1}); and m_c is the mass of catalyst (g).

To confirm whether hydroxyl or superoxide radicals are active species for RhB and indigo carmine degradation, ROS scavenger experiments were performed by employing disodium ethylene diamine tetraacetate dihydrate (EDTA-2Na), isopropanol (IPA), and p-benzoquinone (BQ) at the same concentration of 10 mM as scavengers for holes (q^+), hydroxyl radicals ($\cdot\text{OH}$), and superoxide radicals ($\cdot\text{O}_2^-$), respectively. In addition, EDTA-2Na (Sigma Aldrich) and IPA (Merck, >99.8%) were used in as received condition, while BQ (Sigma Aldrich, 98%) was purified by sublimation under vacuum prior to being used.

2.3. Materials Characterization

The microstructure of the graphitic carbon nitride particles, synthesized through the condensation of melamine, was analyzed using a scanning electron microscope (SEM, Hitachi SU3900 Large chamber, variable pressure SEM) operating at a voltage of 10 kV. A transmission electron microscope (TEM), EOL JEM-2100Plus, was used to conduct a thorough examination of the particle morphology and crystallinity of the material. The piezoelectric properties of the graphitic carbon nitride particles were examined using a piezoresponse force microscope (PFM, NanoManTM VS, Veeco, USA). A conductive Pt/Ir-coated Si cantilever (namely a scanning capacitance microscopy-platinum iridium tip, SCM-PIT) was employed to mount the sample. The PFM tip was applied to a range of DC voltages spanning from -10 to 10 V for hysteresis analysis. For structural analysis, the X-ray powder diffraction analysis was performed using a powder diffractometer (STOE STADI P) double setup fitted with Mythen detectors, using $\text{Cu-K}\alpha_1$ radiation. An SEM-energy-dispersive X-ray spectroscopy (SEM-EDX) scan was performed to determine the composition of the $g\text{-C}_3\text{N}_4$ using a Hitachi SU3900 SEM, with an EDX attached (Ultim Max 170 mm^2).

3. Results and Discussion

3.1. Structural and Microstructural Study

Figure 3a shows an X-ray diffraction (XRD) pattern of the graphitic carbon nitride synthesized through the polycondensation of melamine collected at ambient conditions and Figure 3b,c shows TEM images and selected area electron diffraction (SAED) pattern of $g\text{-C}_3\text{N}_4$, respectively. The XRD reflections exhibit a sharp prominent characteristic peak near $2\theta = 27.43^\circ$, corresponding to $g\text{-C}_3\text{N}_4$.^[33] This peak can be indexed as (002) reflection and corresponding d spacing is calculated to be 0.325 nm . This represents the interlayer structural packing. Another prominent reflection is observed at 13.17° , which can be indexed as the

(100) plane and represents the interplanar separation. This reflection appears due to the in-plane repetition of tri-s-triazine unit cell along the (100) plane and the corresponding calculated interplanar spacing is 0.672 nm .

The measured XRD peaks were compared with the triazine (green lines) and tri-s-triazine (red lines) structures suggested by Teter et al.^[34] and Fina et al.^[33] respectively. The triazine-based unit cell has parameters $a = b = 4.7420 \text{ \AA}$, $c = 6.7205 \text{ \AA}$, $\alpha = \beta = 90^\circ$, and $\gamma = 120^\circ$ in a hexagonal setting ($\overline{P}6m2$ space group), which were proposed by considering the 3D A–B stacking formation. However, in this work, the measured (002) is shifted toward a higher 2θ , suggesting a lower interlayer separation and a shift in the intralayer spacing to 0.411 nm compared to the observed 0.325 nm . Similar results were reported for polymeric carbon nitride.^[35] Starting from the unit cell parameters of Teter et al., Fina et al.^[33] proposed theoretical unit cell parameters of $a = b = 7.113 \text{ \AA}$, $c = 6.490 \text{ \AA}$, $\alpha = \beta = 90^\circ$, and $\gamma = 120^\circ$ by considering a tri-s-triazine stacking framework. The c lattice parameter was chosen to match the interlayer separation, which also closely matches our observed (002) plane. However, this model could not accommodate the (100) and (101) reflections. From the tri-s-triazine structure, Lotsch et al. suggested that the orthorhombic unit cell has parameters $a = 16.7 \text{ \AA}$, $b = 12.4 \text{ \AA}$, $c = 6.49 \text{ \AA}$, and $\alpha = \beta = \gamma = 90^\circ$ with space group: $P2_12_12$ based on the tri-s-triazine structure from an electron diffraction study.^[36] Based on the modifying unit cell parameters suggested by Lotsch et al., Fina et al.^[33] also proposed orthorhombic unit cell of parameters: $a = 16.4 \text{ \AA}$, $b = 12.4 \text{ \AA}$, $c = 6.49 \text{ \AA}$, and $\alpha = \beta = \gamma = 90^\circ$, which provides a closer fit to the measured XRD data, as indicated by the blue lines in Figure 3a.

The SAED pattern of the $g\text{-C}_3\text{N}_4$ in Figure 3c has several clear concentric rings, which indicate the crystalline structure in the graphitic carbon nitrate material. The d spacings of these rings are determined to be 0.210 and 0.123 nm , which closely match the patterns of (200) and (302) reflections. Furthermore, there are diffuse rings found near the centrally located brilliant spot, which correspond to the lower order reflections 001 ($d_{001} = 0.630 \text{ nm}$), 100 ($d_{100} = 0.439 \text{ nm}$), and 002 ($d_{002} = 0.317 \text{ nm}$), possibly resulting from the presence of short-range ordering, see Figure S4, Supporting Information.

Figure 4a,b shows micrographs showing the particle morphology of $g\text{-C}_3\text{N}_4$. The sample appears to have aggregated particles, ranging from 1 to $10 \mu\text{m}$, which are thick and irregularly shaped. They are uniformly dispersed across the whole sample surface. The bulk of the particles have an arrangement of stacked layers with a layered porous structure and rough surfaces also being observed, which is a common occurrence for this material.^[30,37] The material composition of $g\text{-C}_3\text{N}_4$ was shown to be 44.3 at\% carbon and 53.3 at\% nitrogen through investigation using SEM-EDX; see Figure S1, Supporting Information.

3.2. Piezoresponse Force Microscopy Study

The potential piezoelectric properties of the as-produced graphitic carbon nitride particles were investigated with a PFM (NanoMan VS, Veeco, USA), where a conductive Pt/Ir-coated Si cantilever (SCM-PIT) was utilized. Applied DC voltages from -10 to 10 V were applied to the PFM tip for hysteresis analysis

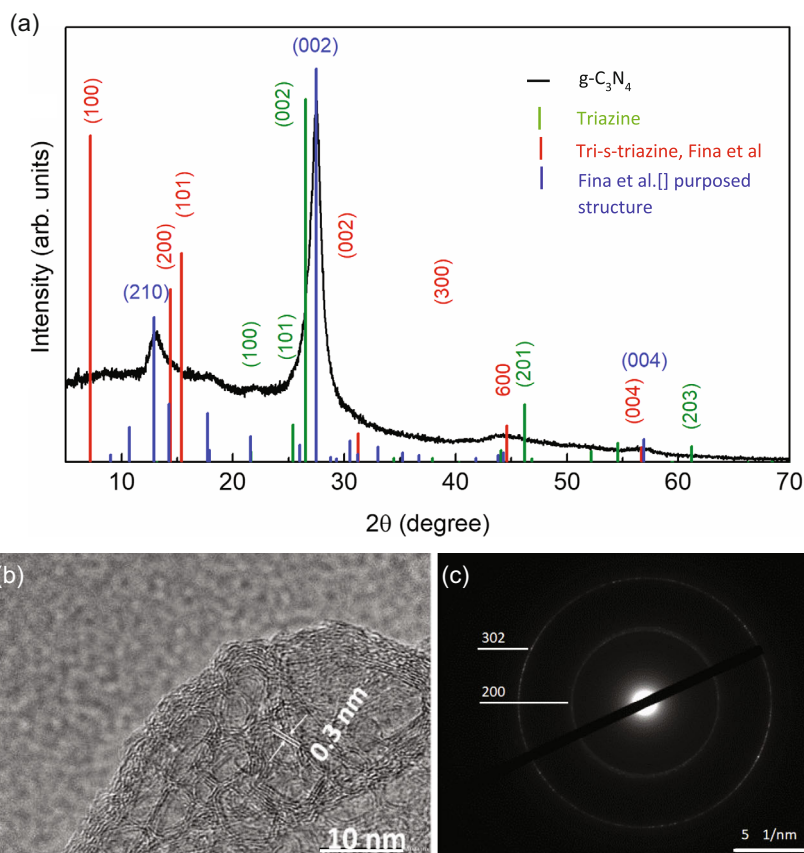


Figure 3. a) XRD pattern of graphitic carbon nitride ($g\text{-C}_3\text{N}_4$). The collected patterns were matched with triazine unit cell parameter $a = b = 4.7420 \text{ \AA}$, $c = 6.7205 \text{ \AA}$, $\alpha = \beta = 90^\circ$, and $\gamma = 120^\circ$ (red) proposed by Teter et al.^[34] and modified tri-s-triazine unit cell parameter $a = b = 13.9246 \text{ \AA}$ and $c = 6.49 \text{ \AA}$ (red) and orthorhombic unit cell of parameters: $a = 16.4 \text{ \AA}$, $b = 12.4 \text{ \AA}$, $c = 6.49 \text{ \AA}$, and $\alpha = \beta = \gamma = 90^\circ$ C proposed by Fina et al. (blue).^[33] b) TEM images of $g\text{-C}_3\text{N}_4$ and c) SAED pattern of $g\text{-C}_3\text{N}_4$.

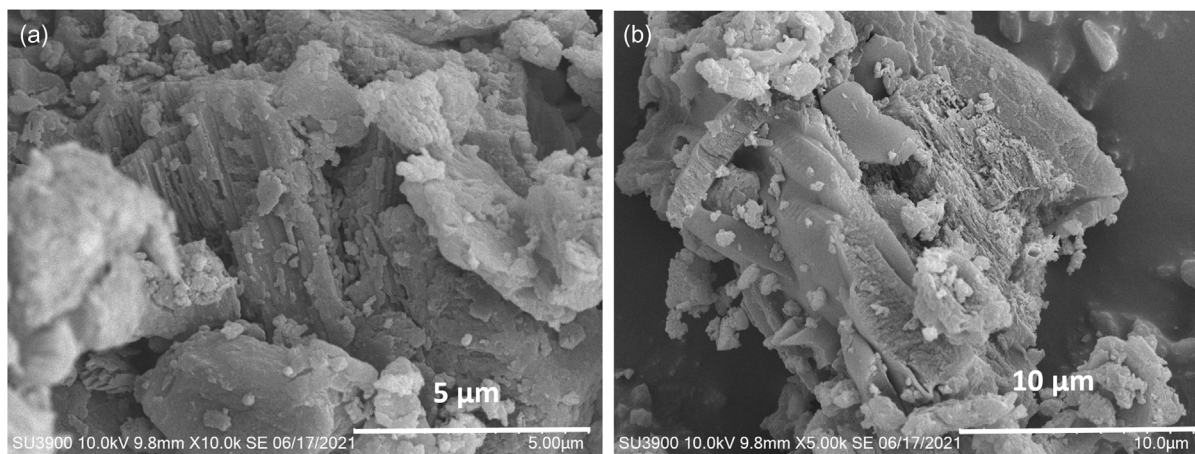


Figure 4. a,b) Scanning electron micrographs of graphitic carbon nitride ($g\text{-C}_3\text{N}_4$).

and undertaking electric-field-dependent measurements while scanning the powder sample surface. **Figure 5** shows the amplitude images (Figure 5a), phase image (Figure 5b), and local hysteresis loop behavior (Figure 5c), which is indicative of piezoelectric activity.^[38] The amplitude difference in Figure 5a

indicates the presence of the spontaneous piezoelectric response, while the contrast between the light and dark regions in Figure 5b shows opposite polarization directions, demonstrating a good piezoresponse. An upward and downward polarization is observed in Figure 5c. The high-piezoresponse amplitude of the

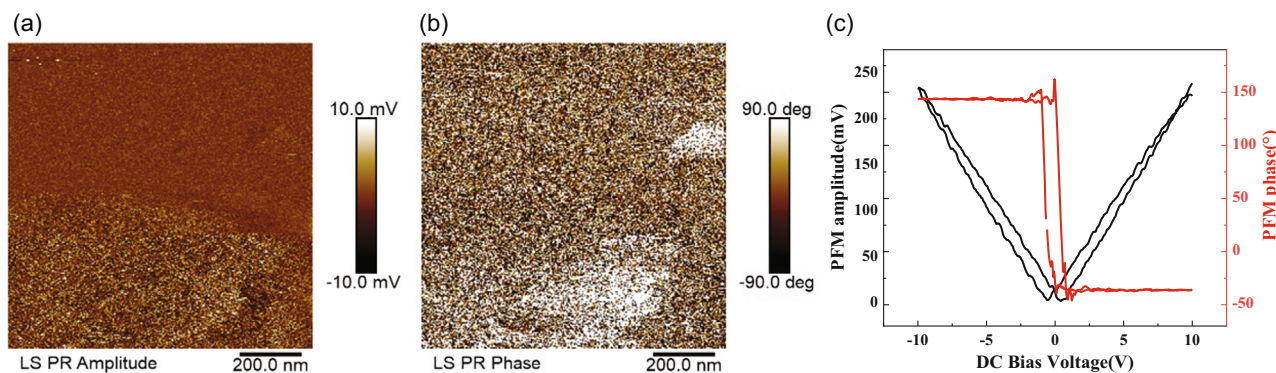


Figure 5. PFM images of the $g\text{-C}_3\text{N}_4$ powders: a) amplitude and b) phase; c) local hysteresis loop behavior for the amplitude and phase.

butterfly loop and the 180° phase angle shift behavior reveal polarization switching.

3.3. Piezocatalytic Study

3.3.1. Effect of Catalyst Dose for H_2O_2 Generation

Figure 6a shows the impact of $g\text{-C}_3\text{N}_4$ catalyst dose on H_2O_2 production (ppm) with time for 100 mL H_2O for a mass of 0–15 mg of $g\text{-C}_3\text{N}_4$ with a 20 mL min^{-1} argon flow. It can be seen that the amount of H_2O_2 produced increases linearly with time and increases with the amount of catalyst up to a dosage of 10 mg of $g\text{-C}_3\text{N}_4$. However, when a higher level of 15 mg of $g\text{-C}_3\text{N}_4$ is used, the amount of H_2O_2 decreases. **Figure 6b** shows, more clearly, the relationship between the catalyst dosage and H_2O_2 production rate (mmol h^{-1}) and yield ($\text{mmol h}^{-1}\text{ g}_{\text{cat}}^{-1}$); this indicates that the H_2O_2 production rate increases with the catalyst amount up to 10 mg, while the H_2O_2 yield significantly decreases with increasing catalyst dosage. This is likely to be due to the addition of a higher amount of catalyst resulting in higher collision probability or agglomeration of the particles which, in turn, leads to a decrease in piezoactivity of the catalyst. Another possible explanation is that high sonochemical bubble

populations can lead to weaker/more complex sonochemical effects;^[39] these results are consistent with previous studies.^[25–28] SEM images of $g\text{-C}_3\text{N}_4$ both before and after the application of ultrasound are given in **Figure S2**, Supporting Information, showing a similar morphological pattern.

3.3.2. Effects of Saturated Gases for H_2O_2 Generation

Figure 7 shows the H_2O_2 production (ppm) with 100 mL H_2O , and $g\text{-C}_3\text{N}_4$ catalyst (0–10 mg) for a range of saturated gases. This includes 20 mL min^{-1} of air (**Figure 7a**), O_2 (**Figure 7b**), a mixture of Ar–air at a 1:1 ratio (**Figure 7c**), and a mixture of Ar– O_2 in 1:1 ratio (**Figure 7d**). These gases were selected to examine their critical roles in the generation of H_2O_2 .^[40] **Figure 7e** shows the H_2O_2 production rate (mmol h^{-1}) with $g\text{-C}_3\text{N}_4$ catalyst amount for different saturated gases. It can be seen that the H_2O_2 production rate increases with an increase in catalyst dosage for 0–10 mg and the production rate increases when Ar–air and Ar– O_2 -saturated gases are used. **Figure 9f** demonstrates that the H_2O_2 production yield ($\text{mmol h}^{-1}\text{ g}_{\text{cat}}^{-1}$) decreases for the highest amount of catalyst and increases under Ar–air and Ar– O_2 ; the highest yield was in the presence of Ar– O_2 and was selected for further study for RhB degradation.

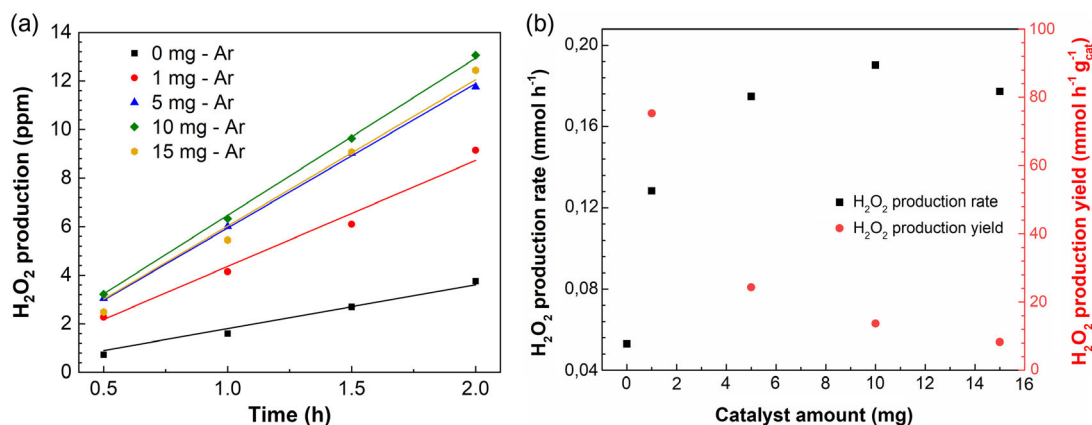


Figure 6. a) H_2O_2 production (ppm) with time, b) H_2O_2 production rate (mmol h^{-1}) and yield ($\text{mmol h}^{-1}\text{ g}_{\text{cat}}^{-1}$) with catalyst amount; conditions are 100 mL H_2O + x mg $g\text{-C}_3\text{N}_4$ + 20 mL min^{-1} argon flow, where $x = 0$ mg to 15 mg.

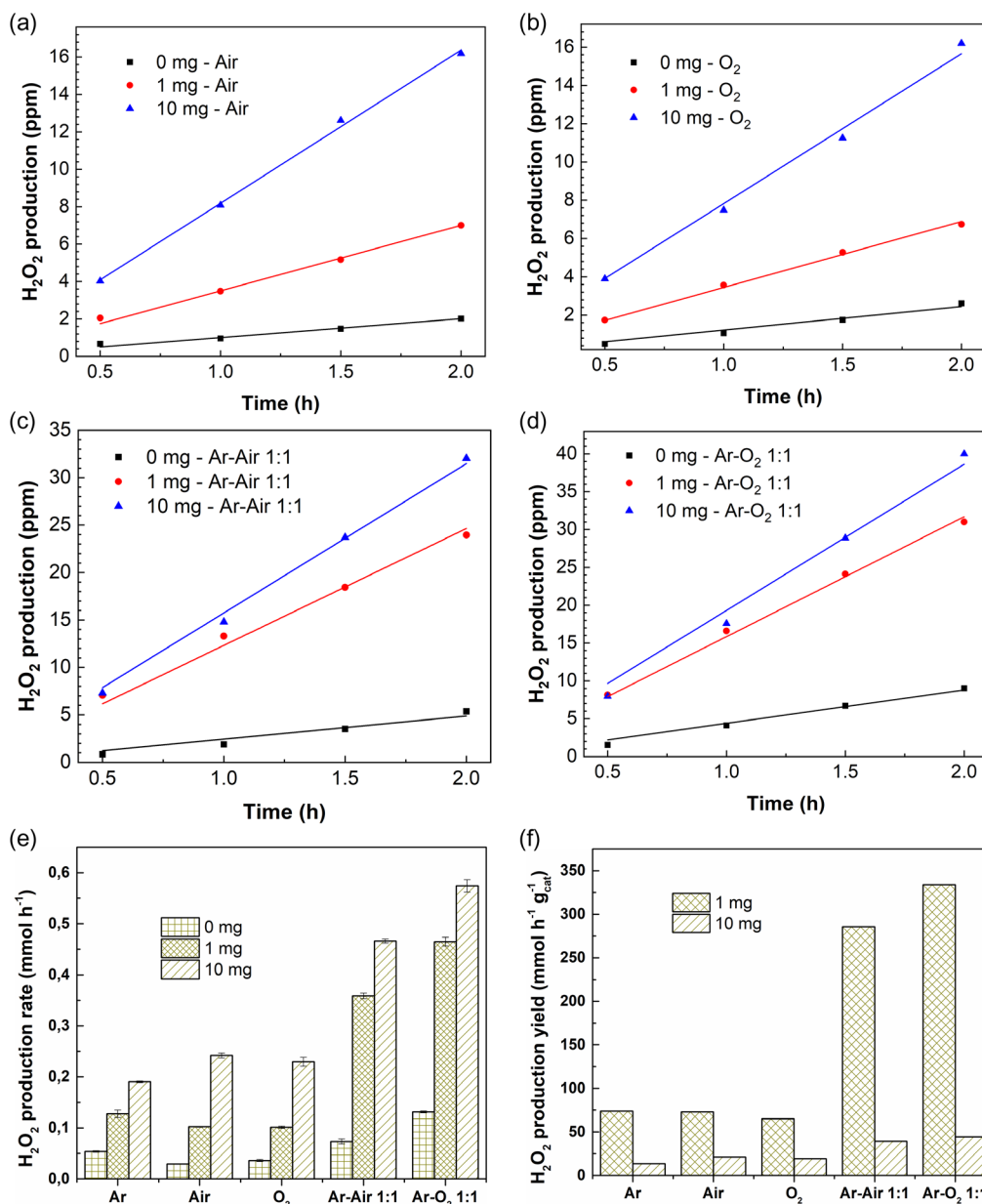


Figure 7. a) H_2O_2 production (ppm) with 100 mL $\text{H}_2\text{O} + x$ mg $\text{g-C}_3\text{N}_4$ catalyst with 20 mL min^{-1} of a) air, b) O_2 , c) mixture of Ar–air in 1:1 ratio, d) mixture of Ar– O_2 flow in 1:1 ratio, e) summary of H_2O_2 production rate (mmol h^{-1}), and f) summary of piezocatalytic production yield of H_2O_2 ($\text{mmol h}^{-1} \text{g}_{\text{cat}}^{-1}$).

3.3.3. Effect of Catalyst Dose on Rhodamine B (RhB) Degradation

Figure 8a shows the impact of $\text{g-C}_3\text{N}_4$ catalyst dose ($x = 0\text{--}15$ mg) on RhB $\ln(C_0/C)$ with time (t); where C_0 is the initial concentration and C is the concentration at time, t . The conditions are 100 mL of H_2O with 5 mg L^{-1} of RhB and x mg of $\text{g-C}_3\text{N}_4$ ($x = 0\text{--}15$ mg) in a 20 mL min^{-1} Ar– O_2 flow. In this case, an Ar– O_2 mixture was selected as it resulted in the highest yield for H_2O_2 generation; see **Figure 7**. A linear relationship between $\ln(C_0/C)$ and time can be observed at all catalyst dosage levels. However, as can be seen more clearly in **Figure 8b**, the RhB degradation rate increases with increasing catalyst dosage up to

10 mg while further increasing the catalyst dosage does not lead to any improvement in RhB degradation rate. **Figure 8b** also shows the relationship between the catalyst amount with initial degradation yield ($\text{mg h}^{-1} \text{g}_{\text{cat}}^{-1}$), again revealing that high levels of catalyst lead to a significant decrease in degradation yield due to a higher collision probability or agglomeration of the catalyst.

3.3.4. Effect of Saturated Gases on RhB Degradation

Figure 9 shows the RhB degradation rate for 100 mL H_2O with RhB $5 \text{ mg L}^{-1} + x$ mg $\text{g-C}_3\text{N}_4$ ($0\text{--}10$ mg) with 20 mL min^{-1} of a

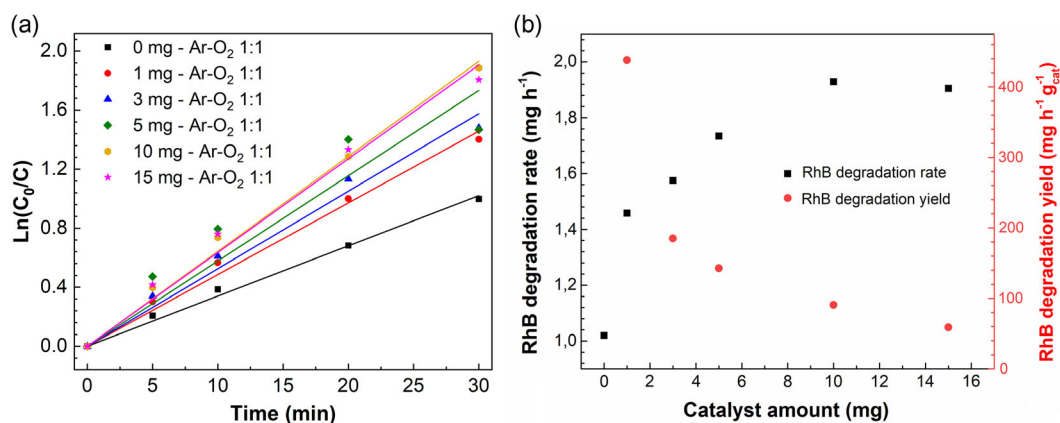


Figure 8. a) Rhodamine B (RhB) degradation, $\ln(C_0/C)$, with time; and b) initial RhB production rate (mg h^{-1}) and yield ($\text{mg h}^{-1} \text{g}_{\text{cat}}^{-1}$) with catalyst amount; 100 mL with RhB 5 mg L^{-1} and $x \text{ mg g-C}_3\text{N}_4 + 20 \text{ mL min}^{-1} \text{ Ar:O}_2$ flow.

range of saturated gases; this includes Ar (Figure 9a), air (Figure 9b), O₂ (Figure 9c), and a mixture of Ar–air flow (Figure 9d). These gases were selected to examine their critical roles in the generation of ROS and RNS, which are responsible for the degradation of dyes. Figure 9e,f summarizes the RhB degradation rate (mg h^{-1}) and yield ($\text{mg h}^{-1} \text{g}_{\text{cat}}^{-1}$), which shows that the rate increases with increasing catalyst dosage while the yield decreases for the highest amount of catalyst. Using oxygen mixed with argon resulted in the highest RhB degradation rate and yield while no obvious enhancement can be observed in the case of mixing argon with air.

3.3.5. Effect of Saturated Gases on Indigo Carmine Degradation

Figure 10 shows the impact of $\text{g-C}_3\text{N}_4$ catalyst dose on change in concentration of indigo carmine with time for 100 mL of H₂O with indigo carmine 25 mg L^{-1} with $x \text{ mg g-C}_3\text{N}_4$ ($x = 0\text{--}10 \text{ mg}$) in 20 mL min^{-1} of a range of saturated gases; this includes Ar (Figure 10a), air (Figure 10b), O₂ (Figure 10c), mixture of Ar–air mix (Figure 10d), and mixture of Ar–O₂ flow (Figure 10e). The mass of x was chosen at 0, 1, and 10 mg since the former is required for the blank experiment while the two later showed the highest piezocatalytic activity on H₂O₂ production and RhB degradation in terms of “yield” and “rate,” respectively.

A linear relationship between $\ln(C_0/C)$ and time is observed. Figure 10f,g summarizes the data for the indigo initial degradation rate (mg h^{-1}) and degradation yield ($\text{mg h}^{-1} \text{g}_{\text{cat}}^{-1}$) again revealing that while high levels of catalyst lead to a slight improved degradation rate, it does not lead to an improved yield. The highest initial degradation rate and yield is achieved for an Ar–O₂ mixture.

3.4. Potential Mechanisms for H₂O₂ and Dye Degradation

3.4.1. Reactions Involved in Sonochemical and Piezocatalytic H₂O₂ Production

Based on the results, it is now possible to propose the sonochemical and piezocatalytic reaction involved $\text{g-C}_3\text{N}_4$ for H₂O₂

production, as can be seen in Figure 11a. It is widely known that vibrations can generate a positive and negative charge on opposing surfaces of a piezoelectric;^[26,41] thus, we can propose reaction as shown in Equation (2) for $\text{g-C}_3\text{N}_4$ during sonication to generate a hole (q^+) and an electron (q^-):

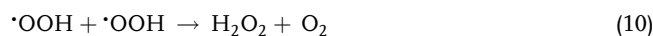


In the presence of argon with no O₂, the key reactions are



An additional *positive* effect of the presence of argon is due to its high polytropic ratio ($\gamma_{\text{N}_2} = 1.4$ while $\gamma_{\text{Ar}} = 1.66$ and $\gamma_{\text{O}_2} = 1.41$), low thermal conductivities ($\lambda_{\text{N}_2} = 0.026 \text{ W mK}^{-1}$ while $\lambda_{\text{Ar}} = 0.018 \text{ W mK}^{-1}$ and $\lambda_{\text{O}_2} = 0.027 \text{ W mK}^{-1}$), and high solubility ($S_{\text{N}_2} = 0.69 \times 10^{-3} \text{ M}$ while $S_{\text{Ar}} = 1.5 \times 10^{-3} \text{ M}$ and $S_{\text{O}_2} = 1.38 \times 10^{-3} \text{ M}$). This can result in a high collapse temperature and large number of nucleation sites for the generation of additional free radicals.

In the presence of oxygen, in addition to Equation (3)–(5), Equation (7)–(11) are also possible. Equation (5) is inhibited in the presence of oxygen due to the occurrence of Equation (10).



The *positive* effect of the presence of oxygen and air is attributed to the generation of H₂O₂ and the additional free radicals from oxygen to form more ROS, as shown in Equation (7)–(11).

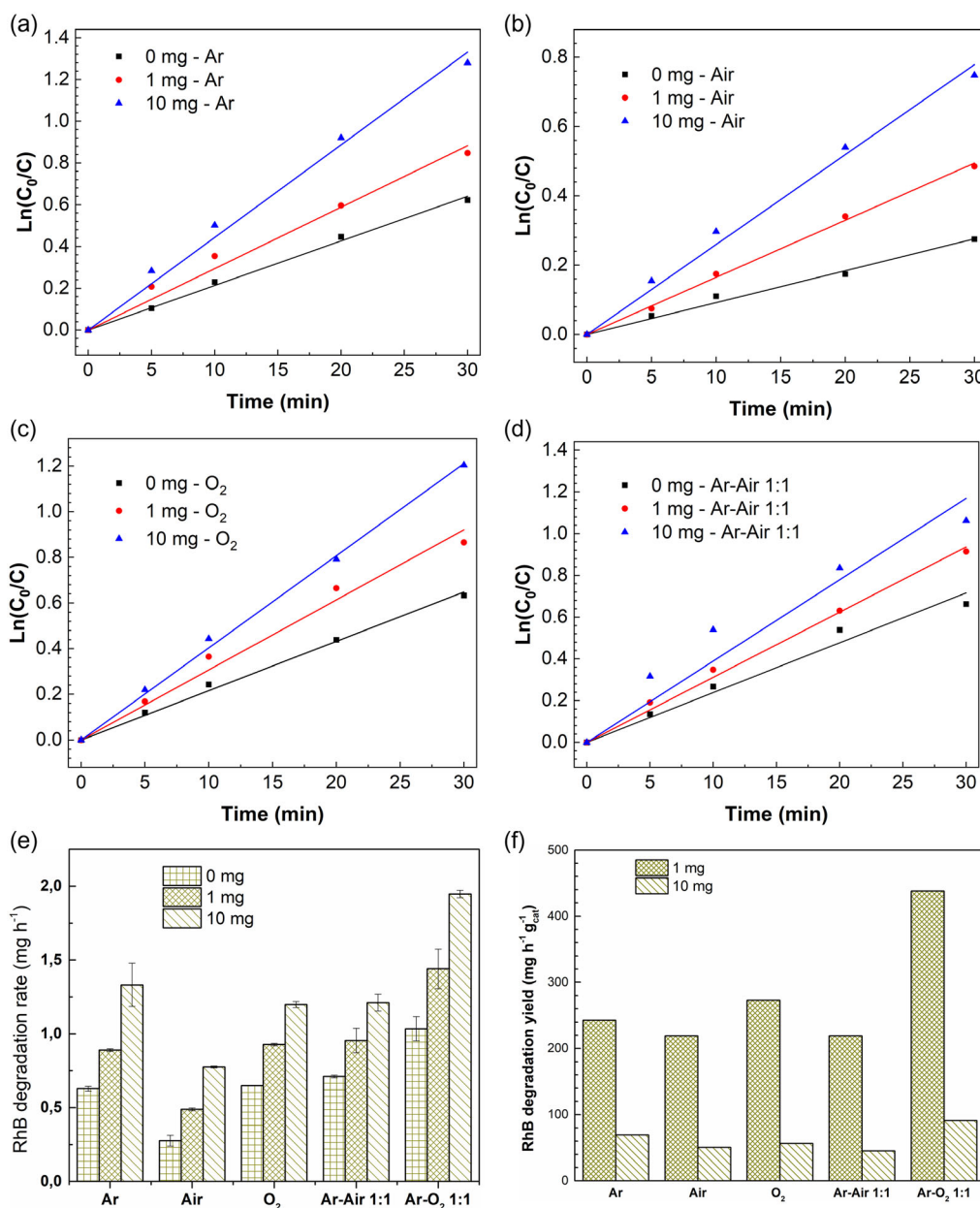


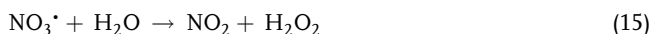
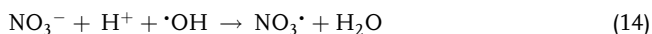
Figure 9. RhB degradation rate 100 mL RhB $5 \text{ mg L}^{-1} + x \text{ mg g-C}_3\text{N}_4$ (0–10 mg) + 20 mL min^{-1} for a) Ar, b) air, c) O_2 , d) mixture of Ar–air flow, e) summary of initial RhB degradation rate (mg h^{-1}), and f) summary of initial piezocatalytic degradation yield of RhB ($\text{mg h}^{-1} \text{g}_{\text{cat}}^{-1}$).

As a result of the additional presence of nitrogen in air, ultrasound-assisted N_2 oxidation to NO_x may occur according to the Zeldovich mechanism, which is similar to that in combustion and shock tube chemistry.^[42] The as-produced NO_x can rapidly react with hydroxyl radicals to generate nitrous and nitric acids as shown in Equation (12) and (13), respectively; this consumption of $\cdot\text{OH}$ can have a negative impact on H_2O_2 production.



An additional *negative* effect of nitrogen in the mixture with argon and oxygen is widely accepted due to its lower polytropic ratio ($\gamma_{\text{N}_2} = 1.4$ while $\gamma_{\text{Ar}} = 1.66$ and $\gamma_{\text{O}_2} = 1.41$), higher thermal conductivity ($\lambda_{\text{N}_2} = 0.026 \text{ W mK}^{-1}$ while $\lambda_{\text{Ar}} = 0.018 \text{ W mK}^{-1}$ and $\lambda_{\text{O}_2} = 0.027 \text{ W mK}^{-1}$), and lower solubility ($S_{\text{N}_2} = 0.69 \times 10^{-3} \text{ M}$ while $S_{\text{Ar}} = 1.5 \times 10^{-3} \text{ M}$ and $S_{\text{O}_2} = 1.38 \times 10^{-3} \text{ M}$). This results in a low collapse temperature and low number of nucleation sites that are necessary for the generation of free radicals.

However, a *positive* effect of nitrogen is attributed to the increased conversion of $\cdot\text{OH}$ radicals to $\text{NO}_3\cdot$ RNS, which is followed by hydrolysis of the as-produced $\text{NO}_3\cdot$ radicals to form H_2O_2 according to Equation (14) and (15), respectively.



Only one mole of $\cdot\text{OH}$ is required to produce one mole of H_2O_2 in the presence of significant H^+ ions, while H_2O_2 production from sonolysis (purely sono-chemical effects) of water requires the recombination of two moles of $\cdot\text{OH}$, see Equation (5).

Therefore, as can be seen in Figure 7, regardless of the presence or absence of $\text{g-C}_3\text{N}_4$, H_2O_2 production rates are almost similar under different atmosphere including argon, air, and

oxygen. However, they are enhanced under mixed gases (Ar-air and Ar- O_2) due to the synergic positive effects of argon, nitrogen, and oxygen.

3.4.2. Reactions Involved in Sonochemical and Piezocatalytic Degradation of Dyes

It is also possible to propose the sonochemical and piezocatalytic reaction involved in the creation of ROS, which are responsible for the degradation of dyes. These reactions are similar to those

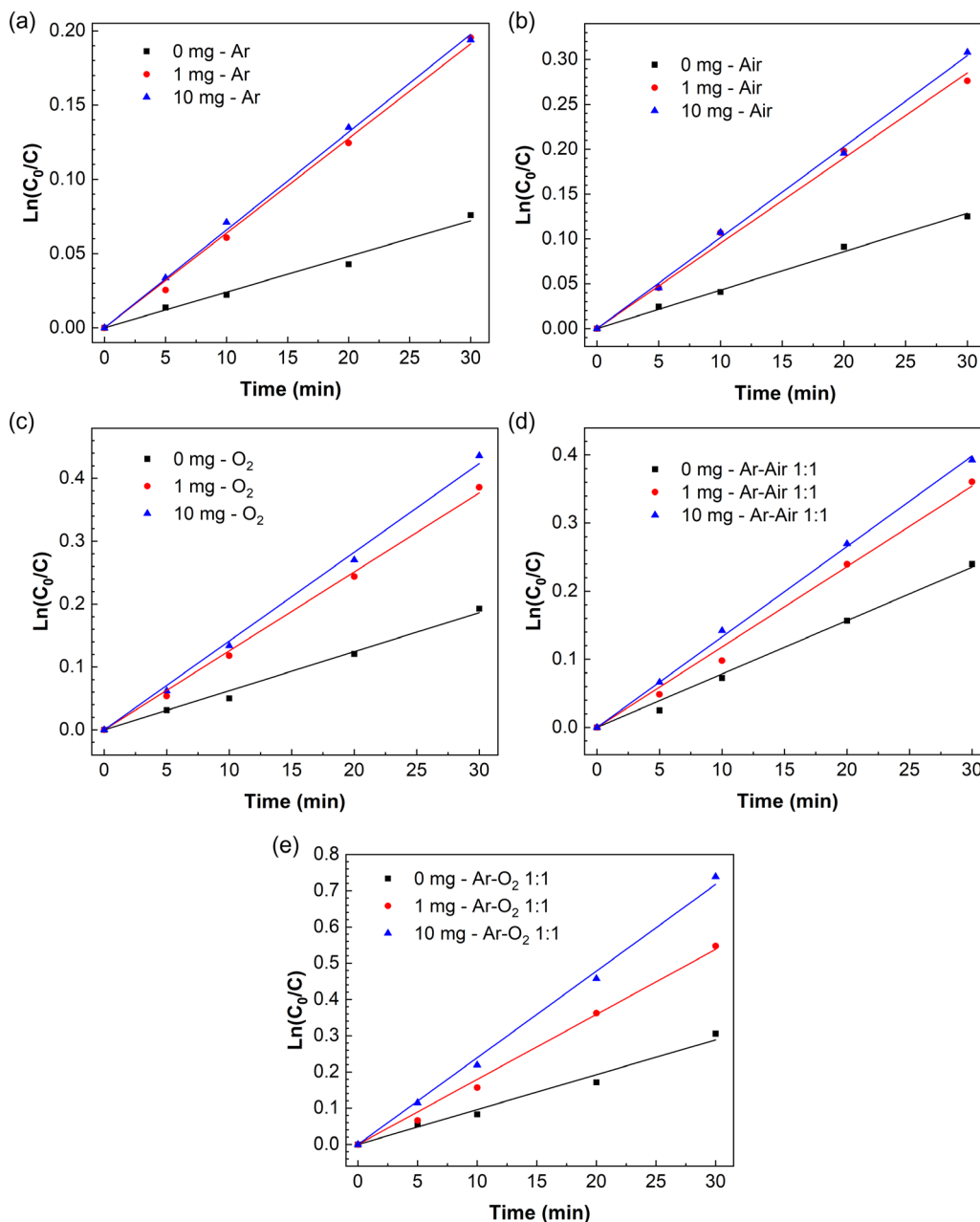


Figure 10. Indigo carmine initial degradation rate 100 mL indigo carmine $5 \text{ mg L}^{-1} + x \text{ mg g-C}_3\text{N}_4$ (0–10 mg) + 20 mL min^{-1} for a) Ar, b) air, c) O_2 , d) mixture of Ar–air flow, e) mixture of Ar– O_2 flow, f) summary of indigo carmine initial degradation rate (mg h^{-1}), and g) summary of piezocatalytic initial degradation yield of indigo carmine ($\text{mg h}^{-1} \text{ g}_{\text{cat}}^{-1}$).

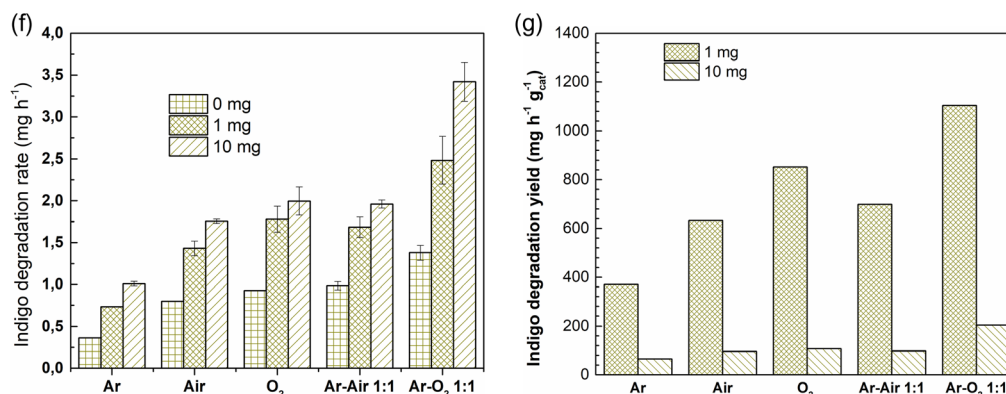


Figure 10. Continued.

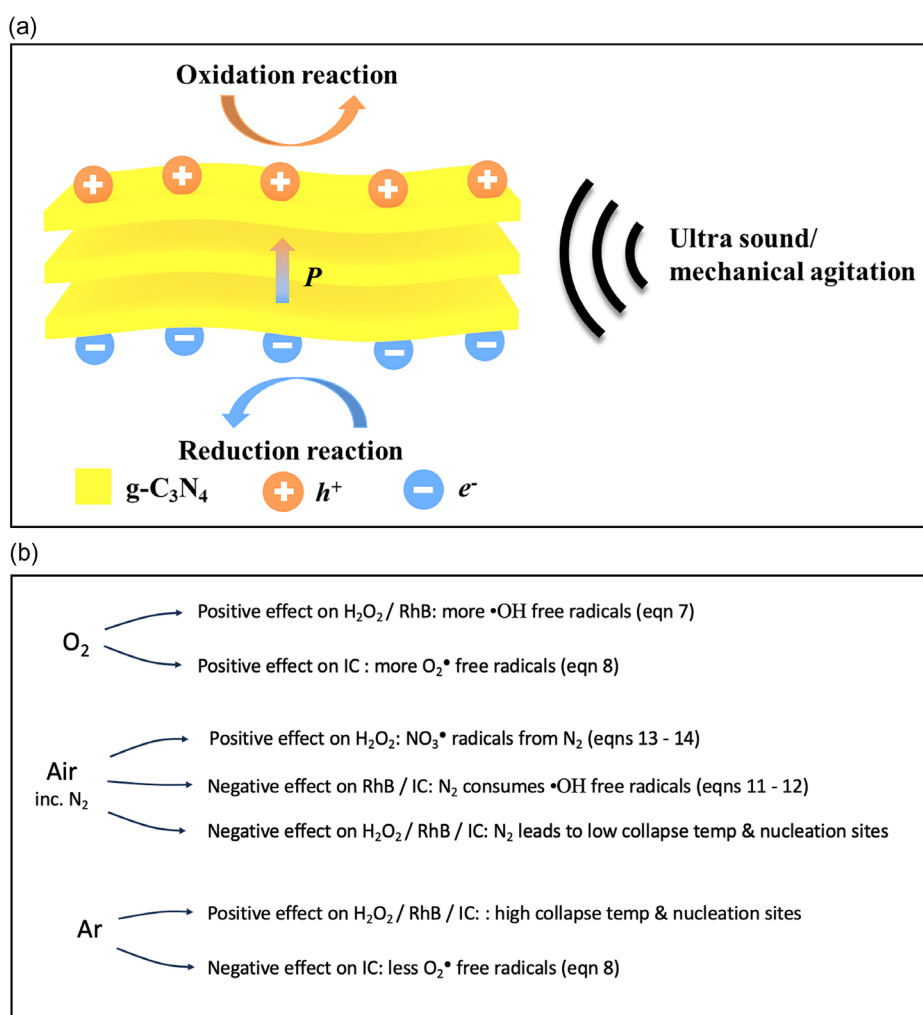


Figure 11. a) Reaction mechanism for piezocatalysis, b) summary of effects of atmosphere on generation of ROS, RNS for hydrogen peroxide production, and degradation of RhB and indigo carmine.

involved in sonochemical and piezocatalytic H₂O₂ production, except for the reactions between the ROS to generate H₂O₂ due to the presence of abundant dye molecules that are capable of scavenging ROS.

Accordingly, in the presence of argon, the key reaction for the generation of ROS is shown in Equation (3) and (4); as described, argon also provides a high collapse temperature and large number of nucleation sites to generate free radicals. In the presence of

argon, there is a negative effect of indigo carmine degradation since the lack of oxygen leads to less $O_2^{\cdot-}$ free radicals.

In the presence of oxygen, there are additional beneficial reactions, in particular Equation (8) and (9) to create ROS to benefit the degradation of RhB and indigo carmine. However, in the presence of nitrogen, hydrogen radicals are consumed through reactions as shown in Equation (12)–(15) to reduce RhB and indigo carmine degradation.

Consequently, the presence of argon and oxygen is more beneficial for the degradation of dyes while the presence of nitrogen in air can decrease the sonochemical and piezocatalytic activity toward dye degradation due to the consumption of generated hydroxyl radicals.

It is worth noting that the anionic dye (indigo carmine) was degraded more rapidly than the cationic dye (RhB) regardless in the presence or absence of g-C₃N₄, except for the case where argon was used as saturated gas. The results are consistent with those reported by Kim and Jo who also studied the photocatalytic decomposition of indigo carmine and RhB over g-C₃N₄.^[43] Since the adsorption ability with both dyes are negligible, the degradation of RhB and indigo carmine is, in this case, only based on the reactivity between the generated ROS and dye molecules. It was reported that $O_2^{\cdot-}$ radicals are the major ROS responsible for the photocatalytic degradation of indigo carmine,^[44] while both $\cdot OH$ and $O_2^{\cdot-}$ are responsible for the piezocatalytic degradation of RhB.^[18] Therefore, the degradation of RhB is least effective under air due to the negative effect of nitrogen on the $\cdot OH$ formation, whereas degradation of indigo carmine is least effective under argon atmosphere.

To demonstrate the mechanism, ROS scavenger experiments were performed by employing EDTA-2Na, IPA, and BQ at the same concentration of 10 mM as scavengers for holes (q+), hydroxyl radicals ($\cdot OH$), and superoxide radicals ($\cdot O_2^{\cdot-}$), respectively. Figure S3a,b indicates that the presence of holes is less important for sono-piezocatalytic degradation of both RhB and indigo carmine, which is in agreement with a previous study.^[45] However, as shown in Figure S3a, Supporting Information, the sono-piezocatalytic activity toward RhB degradation was inhibited significantly by the addition of IPA or BQ, regardless of the gas atmosphere, indicating that both $\cdot OH$ and $\cdot O_2^{\cdot-}$ radicals acted as active species for degradation of RhB. Surprisingly, the scavenging effect of BQ is comparable with that of IPA in the absence of oxygen. Kondo et al. found evidence for superoxide formation during the application of ultrasound in argon-saturated aqueous solution.^[46] They concluded that $\cdot O_2^{\cdot-}$ can be formed directly by the sonolysis of water in the absence of oxygen as long as the temperature of a cavitation bubble collapse is sufficiently high. This can explain why both IPA and BQ are active in the inhibition of sono-piezocatalytic degradation of RhB.

As expected, BQ exhibits the highest scavenging activity in the case of degradation of indigo carmine, confirming that $\cdot O_2^{\cdot-}$ species are responsible for sono-piezocatalytic degradation. The scavenging effect of IPA, however, is more complex. While IPA revealed a minor scavenging effect in argon-saturated solution, its presence significantly enhanced the sono-piezocatalytic degradation rate of indigo carmine in air or Ar–O₂ atmosphere. To our knowledge, the unexpected positive effect of IPA for the degradation of indigo carmine has not been reported elsewhere and is worthy of further study. These observations are

summarized in Figure 11b, which outline the positive and negative effects based on the presence of O₂, air (which includes N₂), and Ar.

4. Conclusions

The effect of saturated gases and catalyst dosage on both H₂O₂ generation and dye degradation is examined using graphitic carbon nitride (g-C₃N₄) as a potential piezoelectric catalyst. The g-C₃N₄ material was characterized in terms of its particle morphology, phase structure, and piezoelectric properties. Using a custom designed double-bath sono-reactor, a detailed catalytic evaluation was carried out to assess the performance of the material for H₂O₂ production and degradation of dyes (RhB and indigo carmine) in the presence of ultrasound. The catalytic performance was assessed for a range of g-C₃N₄ dosage levels and saturated gases. In all cases, a low dosage of catalyst leads to a high yield since the collision probability and agglomeration of the particles in addition to bubble population effects are minimized. A range of gases were chosen due to their important roles in sonochemical production of ROS and RNS to elucidate the potential catalytic mechanism. For H₂O₂ production, the use of an Ar–O₂ mix (1:1) of saturated gas led to the highest H₂O₂ yield; it also led to highest yield for RhB and indigo carmine degradation due to the synergic positive effect of both argon and oxygen in the generation of H₂O₂ and ROS, respectively. The presence of nitrogen, however, negatively influenced the generation of ROS due to its scavenger effect toward $\cdot OH$, in both air and the Ar–air mixture (1:1), which resulted in a lower yield of RhB and indigo carmine degradation compared to oxygen and Ar–O₂, respectively. Opposite results were observed in the case the impact of nitrogen of H₂O₂ generation due to the ability of nitrogen to improve the conversion of $\cdot OH$ into H₂O₂. This work provides new insights of the mechanisms of sonochemical and piezocatalysis in graphitic carbon nitride, demonstrating how judicious selection of dosage and gas can be used to tailor production rate and yield for H₂O₂ production and water treatment.

Supporting Information

Supporting Information is available from the Wiley Online Library or from the author.

Acknowledgements

A.K. and H.D.P.N. contributed equally to this work. This study is supported by the Vietnam Academy of Science and Technology under NCXS02.02/22-23 project. C.R.B. acknowledges support by UKRI Frontier Research Guarantee on “Processing of Smart Porous Electro-Ceramic Transducers - ProSPECT”, project no. EP/X023265/1. A.K. thanks the National Overseas Scholarship, India. Steven Dunn acknowledges support of the Royal Society through the grant IESR2212164.

Conflict of Interest

The authors declare no conflict of interest.

